

Perovskite Core–Shell Nanowire Transistors: Interfacial Transfer Doping and Surface Passivation

You Meng, Zhengxun Lai, Fangzhou Li, Wei Wang, SenPo Yip, Quan Quan, Xiuming Bu, Fei Wang, Yan Bao, Takuro Hosomi, Tsunaki Takahashi, Kazuki Nagashima, Takeshi Yanagida, Jian Lu, and Johnny C. Ho*



Cite This: *ACS Nano* 2020, 14, 12749–12760



Read Online

ACCESS |



Metrics & More



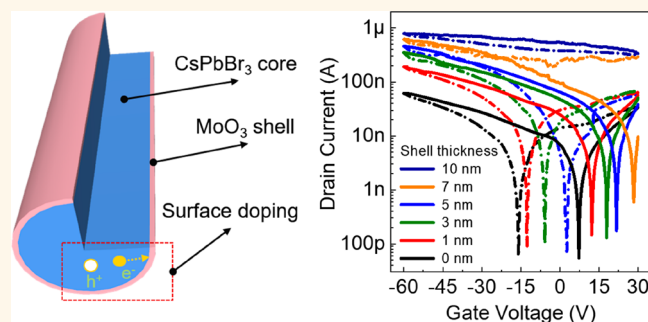
Article Recommendations



Supporting Information

ABSTRACT: While halide perovskite electronics are rapidly developing, they are greatly limited by the inferior charge transport and poor stability. In this work, effective surface charge transfer doping of vapor–liquid–solid (VLS)-grown single-crystalline cesium lead bromide perovskite (CsPbBr_3) nanowires (NWs) via molybdenum trioxide (MoO_3) surface functionalization is achieved. Once fabricated into NW devices, due to the efficient interfacial charge transfer and reduced impurity scattering, a $15\times$ increase in the field-effect hole mobility (μ_h) from 1.5 to $23.3 \text{ cm}^2/(\text{V s})$ is accomplished after depositing the 10 nm thick MoO_3 shell. This enhanced mobility is already better than any mobility value reported for perovskite field-effect transistors (FETs) to date. The photodetection performance of these $\text{CsPbBr}_3/\text{MoO}_3$ core–shell NWs is also investigated to yield a superior responsivity (R) up to $2.36 \times 10^3 \text{ A/W}$ and an external quantum efficiency (EQE) of over $5.48 \times 10^5\%$ toward the 532 nm regime. Importantly, the MoO_3 shell can provide excellent surface passivation to the CsPbBr_3 NW core that minimizes the diffusion of detrimental water and oxygen molecules, improving the air stability of $\text{CsPbBr}_3/\text{MoO}_3$ core–shell NW devices. All these findings evidently demonstrate the surface doping as an enabling technology to realize high-mobility and air-stable low-dimensional halide perovskite devices.

KEYWORDS: surface charge transfer doping, passivation, perovskites, nanowires, transistors



In recent years, because of the potentially high carrier mobility and low defect trap density, single-crystalline halide perovskites and their nanostructures have attracted intensive interest for utilization beyond photovoltaic energy conversion.^{1–3} Combined with the superior optical absorption characteristics, changeable direct bandgap, excellent electroluminescence and tunable ambipolar properties, these perovskites can even be extended to applications in next-generation integrated optoelectronics, such as phototransistors,⁴ light-emitting transistors⁵ and ambipolar transistors,⁶ etc. However, despite the progressive improvements made through various strategies, the achieved figures-of-merits (e.g., field-effect mobility) of halide perovskite field-effect transistors (FETs) to date are still far from the theoretically predicted values.^{7–9} Their poor environmental stability have also substantially impeded the further practical utilization. In this regard, it is urgently required to enhance the charge transport characteristics as well as air stability of halide perovskite electronics.

Generally, the rich surface chemistry and large surface-to-volume ratio of halide perovskite nanostructures would dictate their electrical properties with a significant surface dependence.^{10–12} For instance, there was a pioneer study demonstrating the surface charge transfer doping between hydrogen-terminated diamond (H-diamond) and fullerene (C_{60}) molecules.¹³ Since then, various surface doping schemes have been explored to effectively manipulate the electrical properties of several semiconductor nanostructures, ranging from nanocrystals¹⁴ and nanowires (NWs)¹⁵ all the way to two-dimensional nanomaterials.¹⁶ Among these approaches, there

Received: April 13, 2020

Accepted: September 10, 2020

Published: September 10, 2020



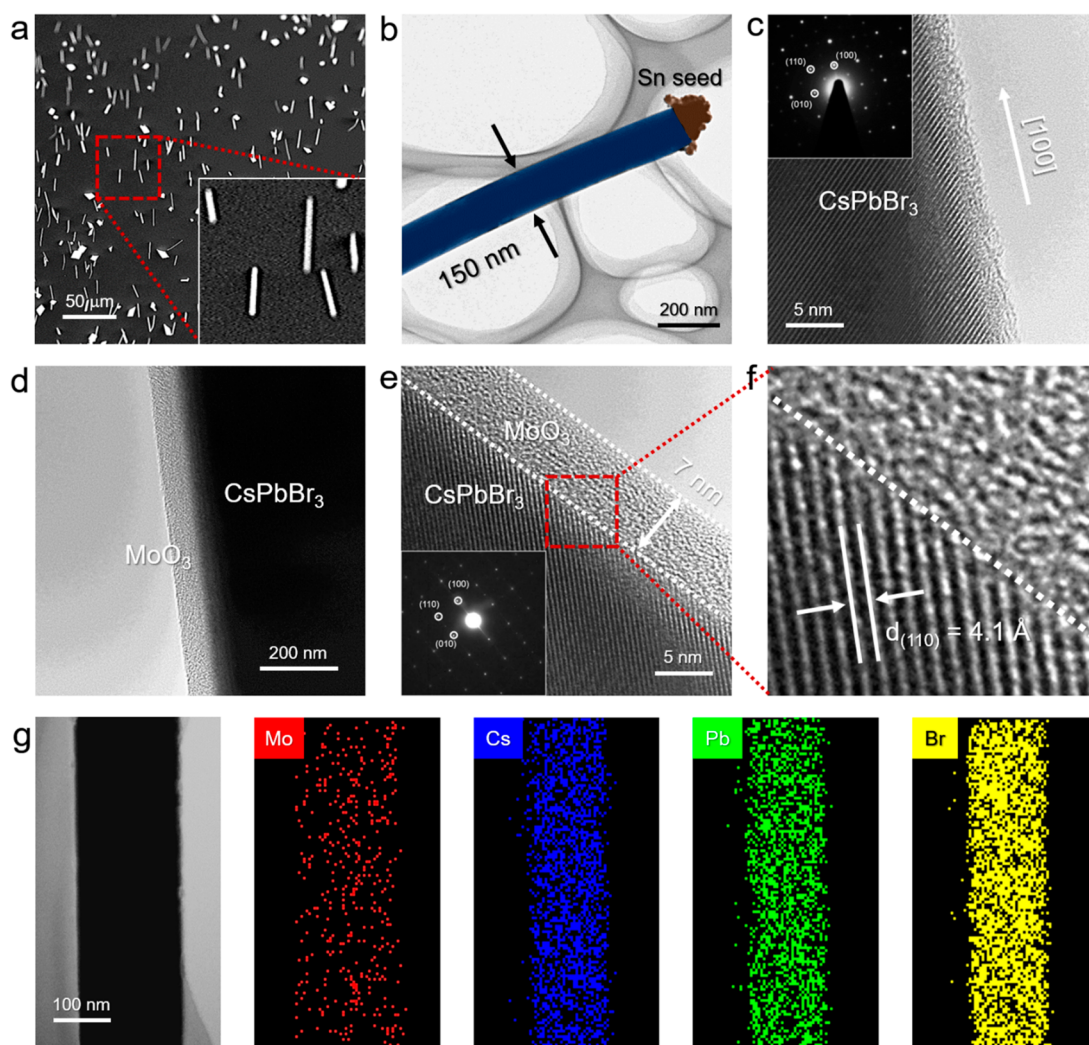


Figure 1. (a) SEM image of vertical CsPbBr₃ NWs grown on Si/SiO₂ substrates. (b) TEM image, (c) HRTEM image, and (inset of c) SAED pattern of a typical VLS-grown CsPbBr₃ NW using Sn as catalysts. (d) TEM image, (e, f) HRTEM images, and (inset of e) SAED pattern of a representative CsPbBr₃/MoO₃ core–shell NW. (g) Scanning TEM image of a typical CsPbBr₃/MoO₃ core–shell NW and corresponding EDS mappings of Mo, Cs, Pb, and Br.

is always a large misalignment of Fermi levels (E_F) between surface dopants and underlying semiconductors, which gives the extraction (or injection) of electrons from (or into) semiconductors to form an electron-deficient (or electron-rich) surface layer on the nanostructures.¹⁷ This can subsequently boost up the device performance of FETs as the device operation relies heavily on the density of charge carriers available in the semiconductor channel. As compared with the conventional substitutional doping, the surface doping is not restricted by the self-compensation effect, low solubility of dopants and formation of deep-level defects associated with host lattice damage; therefore, the electrical properties of device channels and even their conductivity types can be effectively controlled. Importantly, as a noninvasive doping method, surface doping does not introduce any impurity into the host crystal lattice, thereby completely eliminating the charge carrier scattering by ionized dopants for the enhanced carrier mobility. Nevertheless, to the best of our knowledge, there is still no report on the controlled and reliable surface doping of halide perovskite electronic devices at the nanoscale.

Here, we report the realization of high-mobility cesium lead bromide perovskite (CsPbBr₃) NW devices *via* a simple

surface charge transfer doping strategy. Based on the photoemission spectroscopy analysis, it is apparent that the CsPbBr₃ NWs are strongly *p*-type doped by just depositing the molybdenum trioxide (MoO₃) shell layer due to the interfacial electron transfer from CsPbBr₃ NW core to MoO₃ shell. After MoO₃ decoration and device fabrication, the hole mobility of the CsPbBr₃/MoO₃ core–shell NW device is significantly enhanced to 23.3 cm²/(V s), together with a superior responsivity (R) up to 2.36×10^3 A/W and an external quantum efficiency (EQE) of over $5.48 \times 10^5\%$ toward photodetection in the visible region. Importantly, this MoO₃ shell passivation can effectively suppress the environmental degradation of perovskite core as revealed by detailed electron microscopy investigations; as a result, the excellent air stability of CsPbBr₃/MoO₃ core–shell NW FETs is achieved. All these results evidently indicate that it is promising to employ the surface charge transfer doping to improve both electrical performance and environmental stability of future nanostructured halide perovskite devices.

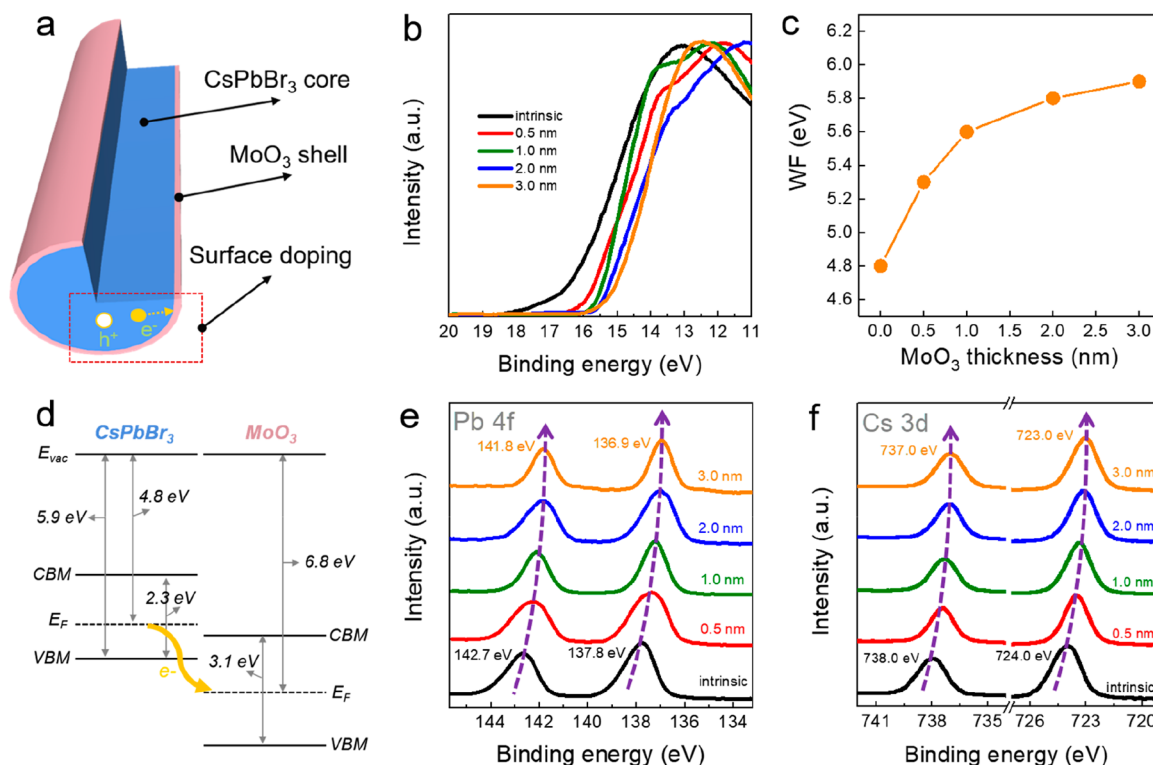


Figure 2. (a) Schematic illustration of the surface charge transfer doping on CsPbBr₃/MoO₃ core–shell NWs. (b) UPS spectra of CsPbBr₃ NWs decorated with various thickness of MoO₃ at the secondary electron cutoff region. (c) Work function evolution of CsPbBr₃ NWs with the increasing MoO₃ thickness. (d) Equilibrium energy-level diagram at the CsPbBr₃/MoO₃ interface. XPS spectra of (e) Pb 4f and (f) Cs 3d peaks of CsPbBr₃/MoO₃ core–shell NWs as a function of MoO₃ thickness.

RESULTS AND DISCUSSION

To start with, pristine CsPbBr₃ NWs are vertically grown on Si/SiO₂ substrates (50 nm thick thermally grown oxide) by using a Sn-catalyzed vapor–liquid–solid (VLS) growth process (Figures 1a and S1).¹⁸ In the case of VLS growth, transient liquid Sn seeds (with a melting temperature of 232 °C, which is below the process temperature of 310 °C) are introduced to facilitate the nucleation kinetics and crystal growth for the precise control on morphology, crystal phase, and surface condition of perovskite NWs obtained on amorphous substrates. As depicted in the transmission electron microscopy (TEM) image in Figure 1b, the catalytic Sn seed is clearly witnessed at the tip of CsPbBr₃ NW, which designates the VLS growth process here. The diameter of grown NWs is observed to be around 150 nm that is consistent with the dimension of Sn nanoparticles employed as catalytic seeds. Owing to the inherent advantages over vapor–solid (VS) growth, the VLS-grown CsPbBr₃ NW exhibits a smooth NW surface without any uncontrolled radial growth along the NW sidewall (Figure S2). As illustrated in the high-resolution TEM image in Figure 1c, there are continuous lattice fringes with a spacing of 4.1 Å corresponding to the (110) plane of cubic CsPbBr₃ crystal, which indicates the single-crystalline nature of CsPbBr₃ NWs fabricated by the VLS process. Also, there is not any distinctive amorphous outer layer formed on the NW surface, confirming the crystallinity of CsPbBr₃ NWs and eliminating the possible influence of the intrinsic outer layer in subsequent surface investigations. The selected-area electron diffraction (SAED) pattern exhibits a 4-fold symmetry with a perfect cubic crystal structure (inset of Figure 1c), which further validates the single crystalline structure. Based on the

SAED patterns collected from multiple NWs, all CsPbBr₃ NWs are grown along the [100] direction. This is mainly due to the fact that the surface free energy of (100) planes is found to be lower than that of other planes of cubic perovskites.^{19,20} All these material characterizations suggest that the VLS-grown CsPbBr₃ NWs possess a clear surface and excellent crystallinity, which gives us an ideal opportunity to study their intrinsic material properties²¹ and hence potentially to explore their high-performance device applications.²²

In this study, MoO₃ is utilized as a surface dopant because of its extremely high work function (WF) of 6.8 eV,^{23,24} ease of low-temperature deposition in vacuum, and excellent chemical stability as compared with other surface dopants (e.g., organic molecules,¹⁶ gas molecules,²⁵ and alkali metals²⁶). In order to deposit the MoO₃ shells on CsPbBr₃ NWs, thermal evaporation is employed with a typical deposition speed of 0.5 Å/s. Specifically, based on the Mo 3d peak analysis in X-ray photoelectron spectroscopy (XPS), the Mo⁶⁺ peaks (corresponding to stoichiometric MoO₃) are dominant in the deposited oxide layer, together with small portions of Mo⁵⁺ peaks occupying around 3% in atomic concentration (Figure S3). Such slightly nonstoichiometric oxide compounds are usually obtained in physical vapor deposition due to the loss of constituent oxygen atoms. In previous experimental and theoretical works,^{27,28} it is understood that nonstoichiometric oxides, such as Mo₂O₅ and MoO₂, can also act as acceptors to withdraw electrons from the underlying semiconductors with a slightly reduced doping efficiency than that of the stoichiometric MoO₃. Hence, to simplify the discussion, only the stoichiometric structure of MoO₃ is focused here. As presented in the HRTEM images in Figure 1d and e, the fabricated CsPbBr₃/MoO₃ NW exhibits a uniform core–shell structure,

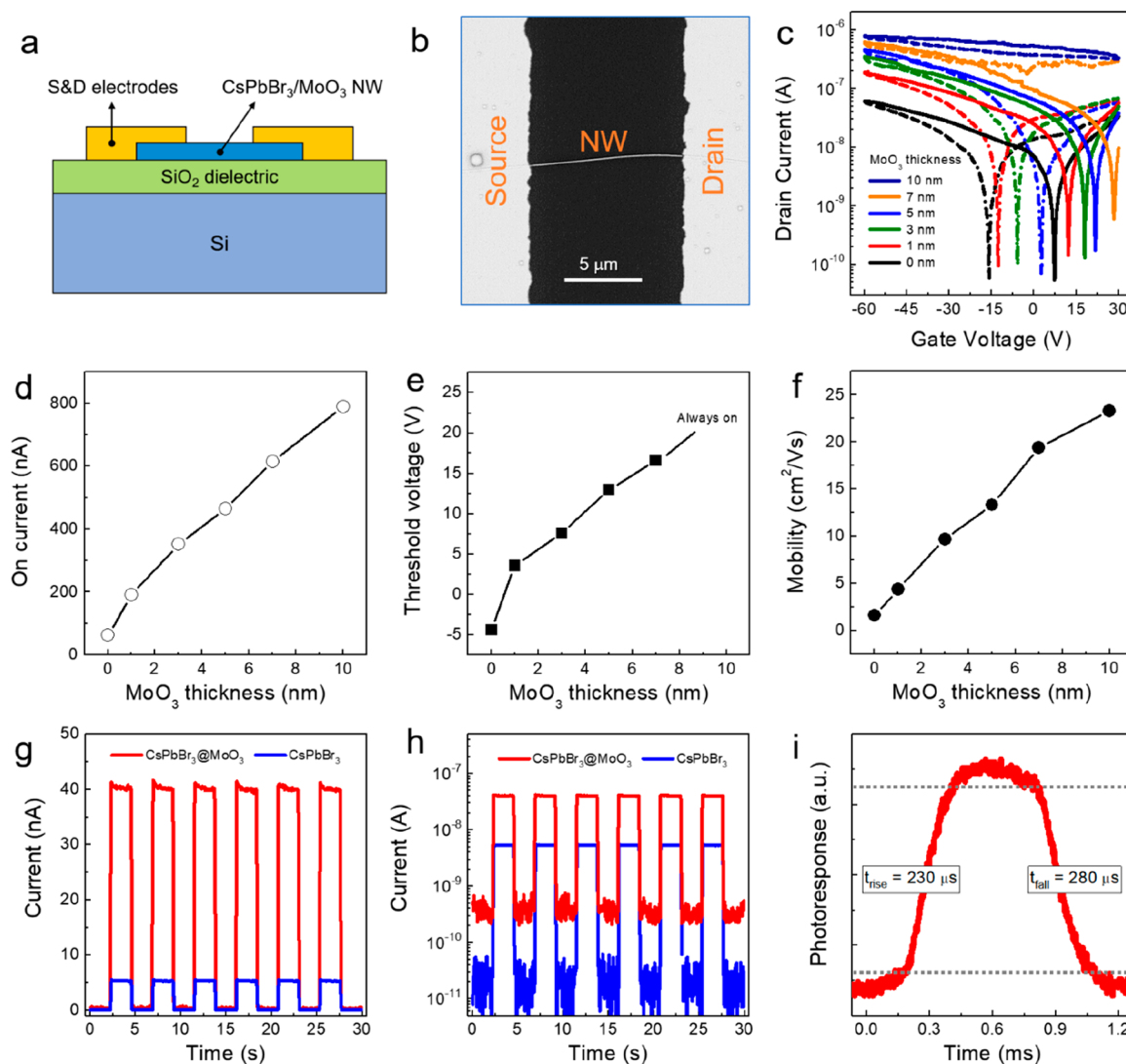


Figure 3. (a) Bottom-gate FET device structure employed in this work. (b) SEM image of the typical device channel. (c) Forward (solid lines) and backward (dashed lines) transfer curves of CsPbBr₃/MoO₃ NW FETs with various MoO₃ thicknesses under a source-drain voltage of 5 V. (d) On current, (e) threshold voltage, and (f) field-effect mobility evolutions of CsPbBr₃/MoO₃ NW FETs with increasing MoO₃ thickness. Device output current as a function of time under the chopped light illumination (1 mW/cm²) with a source-drain voltage of 5 V and a zero gate voltage, using the (g) linear y-axis and (h) logarithmic y-axis. (i) Time-resolved photoresponse of the CsPbBr₃/MoO₃ NW device measurement with a photoresponse measurement circuit.

consisting of a crystalline CsPbBr₃ core and a 7 nm thick amorphous MoO₃ shell (more TEM images can be found in Figure S4). For the crystalline CsPbBr₃ core, there are lattice fringes with a spacing of 4.1 Å (Figure 1f), which agrees the (110) plane of the cubic CsPbBr₃ crystal. This finding is consistent with the (110) plane observed in pristine CsPbBr₃ NWs before MoO₃ deposition, which reveals that the *ex situ* MoO₃ deposition does not alter the crystalline characteristics of underlying CsPbBr₃ cores. The thermally evaporated MoO₃ shells are found to be amorphous, in which this amorphous oxide layer usually has a dense film quality, expecting to block the environmental degradation and thus stabilize the material properties of CsPbBr₃ NWs (Figure S5).²⁴ At the same time, according to the powder X-ray diffraction (XRD) analysis, there are only diffraction peaks of cubic CsPbBr₃ (JCPDS No. 854-0752, *Pm* $\bar{3}m$ (221)) observed, while no diffraction peak can be indexed to MoO₃ because of its amorphous nature (Figure S6). The SAED pattern collected from the CsPbBr₃/MoO₃ core-shell NW also confirms the stable crystalline

structure of the underlying CsPbBr₃ core as well as the amorphous feature of the outer MoO₃ shell (Figure 1e inset). In addition, there is an atomically sharp interface existing between the CsPbBr₃ core and MoO₃ shell, which indicates that no noticeable interfacial chemical reactivity or mutual dissolution occurred at the CsPbBr₃/MoO₃ interface (Figure 1f), further highlighting the excellent chemical stability of MoO₃ and the intact NW core-shell structure. After that, energy-dispersive X-ray spectroscopy (EDS) mapping was also performed to directly evaluate the core-shell NW structure, where Mo is found to be uniformly distributed throughout the entire NW surface while Cs, Pb, and Br are concentrated near the NW core with an ideal Cs/Pb/Br composition ratio of 1:1:3 (Figure S7). From the detailed EDS studies, uniform elemental distribution of Mo (~11 atomic%) was verified on different positions along the length of the CsPbBr₃/MoO₃ core-shell NW (Figure S8), indicating the uniform coverage of MoO₃ shells on the CsPbBr₃ NW cores. The stability enhancement and electrical property improvement associated

Table 1. Key FET Performance Parameters of CsPbBr₃/MoO₃ Core–Shell NW FETs with Increasing MoO₃ Thickness

MoO ₃ thickness [nm]	I_{on} [nA]	V_{th} [V]	$I_{\text{on}}/I_{\text{off}}$	SS [V/decade]	μ_{h} [cm ² /(V s)]	n_{h} [cm ⁻³]
0	62	-4.4	1.1×10^3	2.7	1.5	5.92×10^{18}
1	191	3.6	1.0×10^3	1.9	4.4	6.05×10^{18}
3	352	7.6	1.9×10^3	2.0	9.7	7.18×10^{18}
5	464	13.0	5.2×10^3	1.8	13.3	7.75×10^{18}
7	615	16.6	0.6×10^3	2.1	19.4	8.13×10^{18}
10	790	>30			23.3	$>9.55 \times 10^{18}$

with the core–shell NW structure will be thoroughly discussed in later sections.

In principle, the MoO₃ shell that possesses high WF is capable of withdrawing electrons from the low-WF CsPbBr₃ core, leading to the accumulation of positive charges in the CsPbBr₃ core.^{27,29} As a result, the E_{F} of CsPbBr₃ would shift toward the valence band edge after surface modification with MoO₃, along with the large enhancement of WF. Ultraviolet photoemission spectroscopy (UPS) is then utilized as a powerful technique to directly assess the energy levels at the surface as well as at the core–shell interface of obtained NWs. In detail, thickness-dependent UPS measurements of CsPbBr₃/MoO₃ core–shell NWs with varied MoO₃ shell thickness are performed to evaluate the interfacial charge transfer between the core and shell layers (Figure 2a). Due to the detection limit of UPS, the moderate thickness of a MoO₃ layer up to 3 nm is studied here. With the increasing coverage of the MoO₃ layer on CsPbBr₃ NWs, the secondary electron cutoff would gradually move toward the lower binding energy (Figure 2b), which indicates a shift of E_{F} within the gap toward the valence band maximum (VBM) of CsPbBr₃ accordingly. By linearly extrapolating the secondary electron cutoff region, the WFs of CsPbBr₃ are measured to significantly increase from 4.8 eV for pristine CsPbBr₃ all the way to 5.9 eV with decoration of 3 nm thick MoO₃ (Figure 2c). In this case, the doping efficiency of depositing an ultra-thin MoO₃ layer is expected to be the highest, whereas this efficiency would drop rapidly as the MoO₃ coverage increases. Such a saturation phenomenon of the charge transfer process has also been widely reported in experimental and theoretical works in other material systems.^{23,24,27,29,30} Overall, the increasing WF of CsPbBr₃ with enhanced MoO₃ coverage is a direct indication of the interfacial electron transfer from the CsPbBr₃ core to the MoO₃ shell.

Furthermore, the surface doping of CsPbBr₃ NWs can also be most easily understood in terms of energy band diagrams. As depicted in Figure 2d, when the physical contact is formed between MoO₃ shell and CsPbBr₃ NW core, the large WF difference between MoO₃ (~6.8 eV) and CsPbBr₃ (~4.8 eV) would drive the spontaneous electron transfer from CsPbBr₃ to MoO₃.²³ Meanwhile, the accumulation of delocalized holes in CsPbBr₃ results in the upward energy level bending from the bulk to the surface. This phenomenon was experimentally investigated and further confirmed through XPS analysis in this work (Figure 2e and f). All the XPS peaks are calibrated by using the containment carbon (C 1s) reference at 284.8 eV (Figure S9). For pristine CsPbBr₃ NWs, the peaks located at ~142.7 and ~137.8 eV can be attributed to the Pb 4f_{5/2} and Pb 4f_{7/2} core levels, respectively (Figure 2e), while the paired peaks located at ~724.0 and ~738.0 eV can be ascribed to the Cs 3d_{5/2} and Cs 3d_{3/2} core levels, respectively (Figure 2f).³¹ With the increasing MoO₃ thickness, the positions of the paired Pb 4f peaks as well as paired Cs 3d peaks gradually shift

toward the lower energy values. To be specific, after 3 nm thick MoO₃ decoration, the maximum shifts of Pb 4f and Cs 3d peaks are measured to be ~0.9 and 1.0 eV, accordingly. The clear downshifts of these peaks are consistent with an upward band bending expected after interfacial transfer doping. As shown in the schematic of energy level diagram in Figure S10, the accumulation of delocalized holes sets up a space charge region at the CsPbBr₃ side of the CsPbBr₃/MoO₃ interface, resulting in an upward band bending. Overall, the XPS study also confirms the *p*-type doping of CsPbBr₃ via MoO₃ surface decoration. Based on the proposed mechanism, other transition metal oxides, including WO₃, CrO₃, ReO₃, and V₂O₅, that have the high WFs of 6.7, 6.8, 6.8, and 7.0 eV, respectively,^{27,29,30} can also be applied as electron-withdrawing surface dopants in a way analogous to MoO₃ (detailed energy level values are summarized in Table S1), in which all these are highly desirable to be explored in the near future.

To directly shed light on the carrier transport properties, bottom-gate FETs are constructed by using individual CsPbBr₃/MoO₃ core–shell NWs as the device channel (Figure 3a). A contact transfer method is first utilized to configure CsPbBr₃/MoO₃ core–shell NWs onto device substrates with the SiO₂ dielectric layer (Figure S11).³² Then, the Au source/drain (SD) electrode deposition is performed by thermal evaporation with the assistance of a shadow mask (Figure 3b). First, the contact resistance between SD electrodes and channel layers was estimated by using a simple transmission line method (Figure S12), where a relatively small contact resistance (~2 M Ω) is obtained, suggesting only a small voltage drop existed on the contact. This ensures that the parameters estimated from the transfer curves here can represent the reliable device performance of the NW devices. Figure 3c demonstrates the dual-sweep transfer curves of fabricated CsPbBr₃/MoO₃ core–shell NW devices with increasing MoO₃ thickness from 0 to 10 nm. The corresponding FET performance parameters are summarized in Table 1 and will be discussed in details below. It is obvious that the pristine CsPbBr₃ NW device exhibits an ambipolar transfer characteristic with an on/off current ratio of ~10³, which is possibly due to the balanced effective mass of holes and electrons of CsPbBr₃ NWs being similar to those in previous reports on perovskite-based ambipolar transistors.^{5,33–35} With MoO₃ deposition, the transfer characteristics of FET devices yield a dominant *p*-type behavior with increasing conductance for the decreasing gate voltage (V_{g}). The representative *p*-type output curves are shown in Figure S13, simply implying that the injected holes via surface doping dominate the carrier transport in the device channel. In detail, the transfer curve of the pristine CsPbBr₃ NW device without any MoO₃ decoration presents an on current (I_{on}) of 62 nA at a negative V_{g} of -60 V. As the thickness of MoO₃ increases to 10 nm, the I_{on} gradually increases to 790 nA under the same bias (Figure 3d). The *I*-*V* measurements with a zero gate bias

Table 2. Performance Summary of FETs Based on Halide Perovskites

material	crystallinity	morphology	temperature	mobility [$\text{cm}^2/(\text{Vs})$]	year	ref
(PEA) ₂ SnI ₄	polycrystalline	thin film	RT	$\mu_h = 0.5$	1999	40
MAPb(I/Cl) ₃	polycrystalline	thin film	RT	$\mu_h = 1.24, \mu_e = 1.01$	2015	33
MAPbI ₃	polycrystalline	thin film	78 K	$\mu_h = 2.1 \times 10^{-2}, \mu_e = 7.2 \times 10^{-2}$	2015	5
MAPbI ₃	crystal	microplate	77 K	$\mu_e = 1$	2015	38
(PEA) ₂ SnI ₄	polycrystalline	thin film	RT	$\mu_h = 15$	2016	41
MAPbI ₃	crystal	thin film	78 K	$\mu_h = 2.1$	2016	34
MAPbI ₃	crystal	microplate	77 K	$\mu_e < 0.8$	2016	2
(Cs/MA/FA)Pb(Br/I) ₃	polycrystalline	thin film	RT	$\mu_h = 2.1, \mu_e = 2.5$	2017	42
MAPbI ₃	crystal	microplate	77 K	$\mu_e = 4$	2017	6
MAPbI ₃	crystal	thin film	RT	$\mu_h = 4.7, \mu_e = 2.6$	2018	35
MAPbBr ₃	crystal	thin film	RT	$\mu_h = 3.6$	2018	35
MAPbCl ₃	crystal	thin film	RT	$\mu_h = 3.8$	2018	35
CsPbI ₃	crystal	nanowire	RT	$\mu_h = 3.05$	2019	18
CsPbBr ₃	crystal	nanowire	RT	$\mu_h = 2.17$	2019	18
CsPbCl ₃	crystal	nanowire	RT	$\mu_h = 1.06$	2019	18
CsPbBr ₃	crystal	nanowire	RT	$\mu_h = 1.5$		this work
CsPbBr ₃ @MoO ₃	crystal	nanowire	RT	$\mu_h = 23.3$		this work

were also performed on CsPbBr₃/MoO₃ NW devices. The output current shows a consistent trend with the increasing MoO₃ thickness (Figure S14). Moreover, thin film transistors using a 50 nm thick MoO₃ layer as device channel do not exhibit decent FET performance but show relatively high resistance (*i.e.*, low current in Figure S15), which rules out the possibility that MoO₃ shells act as conducting pathways in CsPbBr₃/MoO₃ core-shell NW transistors. Therefore, the significant increase of I_{on} suggests a significant *p*-type doping effect on the MoO₃-decorated CsPbBr₃ NW induced by the interfacial electron transfer from CsPbBr₃ to MoO₃.¹⁷

Simultaneously, the *p*-type doping effect can also be indicated by the device threshold voltage (V_{th}) shift toward positive voltages with the increasing MoO₃ thickness (Figure 3e). For example, for CsPbBr₃ NWs with the MoO₃ shell thickness ranging from 0, 1, 3, 5, to 7 nm, their device V_{th} values are found to be -4.4, 3.6, 7.6, 13.0, and 16.6 V, respectively, together with distinct on/off current ratios of all around 10³. However, for the case of the 10 nm MoO₃ decorated CsPbBr₃ NW device, it exhibits a metal-like conductivity; therefore, it cannot be completely turned off such that its V_{th} value is undetermined for the measured gate bias range (V_g) range. Such “always on” device operation can be attributed to the excess hole concentration of the MoO₃-decorated CsPbBr₃ NWs that cannot be fully depleted by the gate bias. Technically, for a *p*-type semiconductor channel, the V_{th} values are always dictated by the available free hole concentration (n_h) of the device. This hole concentration can be determined with the analytical expression of $n_h = 4C_g(V_g - V_{\text{th}})/\pi q d^2 L$,³⁶ where d is the NW radius, L is the channel length, and C_g is the gate capacitance. C_g is obtained from the finite element method by using COMSOL MultiPhysics tailored for a cylinder-on-plane model (Figure S16). For a typical CsPbBr₃/MoO₃ NW with a diameter of 160 nm and a channel length of 10 μm , the gate capacitance is determined to be ~ 0.183 fF when using a 270 nm thick SiO₂ layer as the gate dielectric. As depicted in Figure S17, the n_h values are observed to clearly increase from 5.92×10^{18} to $>9.55 \times 10^{18} \text{ cm}^{-3}$ with the deposition of MoO₃ gradually increasing from 0 to 10 nm. It is commonly accepted that the increased n_h value induced by surface doping here is accountable for the downshift of E_F and consequently yields the semiconductor-to-metal transition

when E_F moves below the VBM of CsPbBr₃. As a result, the effect of surface charge transfer doping is proven to be strong enough to fully convert the conductivity of CsPbBr₃ NWs from ambipolar to dominant *p*-type and even to all the way to metallic behavior.

Moreover, the field-effect hole mobility (μ_h) of these devices can be determined using the equation $\mu_h = L^2 g_m / (C_g V_d)$,³⁷ where g_m denotes transconductance that is defined as dI_d/dV_g . As a common feature of perovskite devices, there is a noticeable hysteresis observed in the dual-sweep transfer curves of our devices. Many mechanisms associated with trapping/detrapping, ion migrations, ferroelectric polarization, and so forth have been proposed to explain this hysteresis phenomena.^{2,5,38} In any case, the existence of hysteresis would introduce uncertainty errors in the mobility determination. The forward gate sweep underestimates the μ_h value, while the backward gate sweep imposes a significant overestimation on μ_h .³⁸ To properly evaluate the carrier mobility, we extracted the μ_h values based on the forward-sweep transfer characteristics; this way, the μ_h values extracted in this work would represent a reliable lower bound value. For example, the μ_h of the CsPbBr₃/5 nm MoO₃ NW is determined to be 13.3 and 18.6 $\text{cm}^2/(\text{V s})$ for the forward and backward gate sweeps, respectively. We used the lower bound value of 13.3 $\text{cm}^2/(\text{V s})$ in our analysis. As displayed in Figure 3f, the μ_h values steadily increase for the increasing MoO₃ thickness from 0 to 10 nm. In particular, these CsPbBr₃/MoO₃ core-shell NW devices present an almost 15 \times enhancement of μ_h from 1.5 $\text{cm}^2/(\text{V s})$ for the pristine CsPbBr₃ NW all the way to 23.3 $\text{cm}^2/(\text{V s})$ after a 10 nm thick MoO₃ coating, suggesting the improved hole transport in the CsPbBr₃ NW channel. Importantly, this enhanced μ_h value is already higher than any mobility value reported for perovskite FETs to date (Table 2). The significant mobility enhancement of surface-doped core-shell NW devices can be attributed to three main reasons: (1) The spontaneous interfacial charge transfer largely increases the free hole concentration in CsPbBr₃, effectively filling the trap sites as well as screening the trapped charges. This is beneficial to the improved carrier transport in semiconductor channels under bias, as the operation of the FET device is mainly limited by the trapped charge scattering in device channels.³⁹ (2) In contrast to conventional substitutional doping, surface

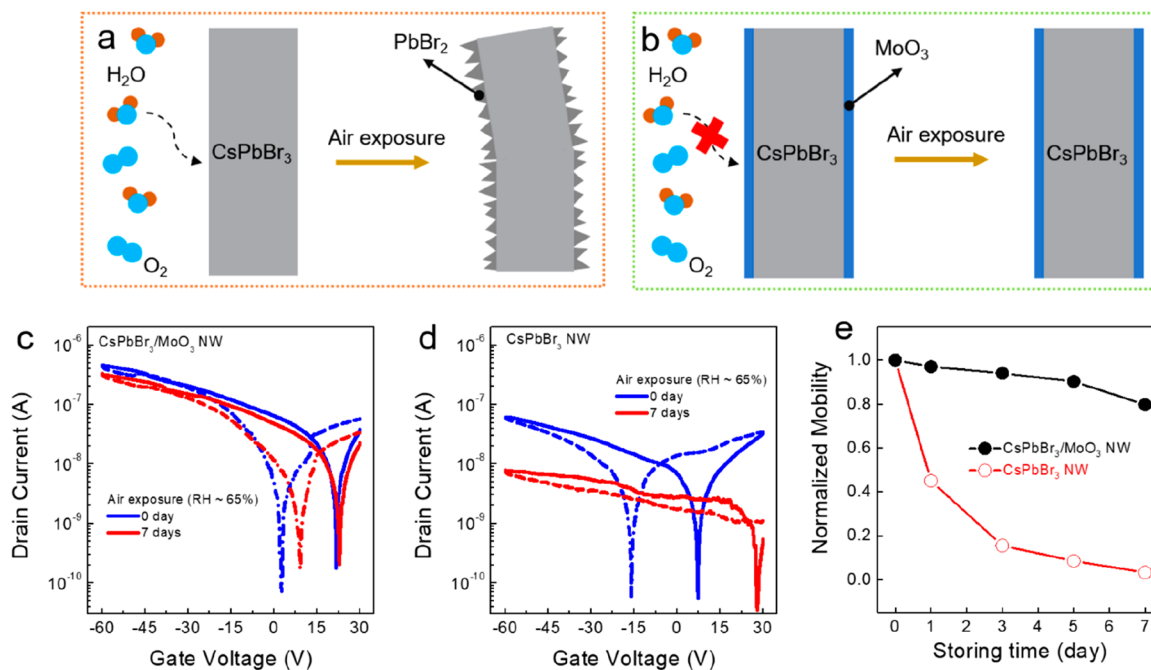


Figure 4. (a) Proposed degradation mechanism of CsPbBr₃ NWs and (b) stability enhancement mechanism of CsPbBr₃/MoO₃ core-shell NWs at ambient conditions. Forward and backward transfer curves of the (c) CsPbBr₃/MoO₃ NW and (d) pristine CsPbBr₃ NW with different durations of storage. (e) Mobility of the CsPbBr₃/MoO₃ NW and CsPbBr₃ NW FETs with increasing duration of storage.

doping would not introduce any impurity atoms into the host crystal lattice, thereby reducing the carrier scattering centers.²⁴ Due to the spatial separation of the dopants from the carriers, the corresponding ionized impurity (acceptor) scattering is completely minimized, which gives the superior hole mobility for CsPbBr₃/MoO₃ core-shell NWs. (3) With the rational design of core-shell NW configuration, the defect-free single crystalline nature of the VLS-grown CsPbBr₃ NW core as well as the chemically stable MoO₃ shell would guarantee improved intrinsic device performance without any performance degradation induced by external environmental factors.

To further investigate the fundamental charge transport properties of individual perovskite core-shell NWs, temperature dependent electrical measurements of the NW devices were carried out and compiled in Figure S18. In specific, there are two different temperature regimes identified from the distinct slopes in the mobility (μ) versus temperature plots, which are analyzed by fitting a typical power law behavior of $\mu \sim T^{-\gamma}$. In the high-temperature regime ($150 \text{ K} < T < 298 \text{ K}$), the exponent γ values are found to be roughly the same for both CsPbBr₃/5 nm MoO₃ NW and CsPbBr₃ NW devices, which means that there are similar thermally activated carrier transport processes in these NW devices. In fact, consistent phenomena have also been reported in a similar temperature regime, where the charge transport in lead halide perovskites is dominated by the ion migration, polarization disorder of A-site cations and phonon scattering.^{43,44} In the low-temperature regime ($78 \text{ K} < T < 150 \text{ K}$), the CsPbBr₃ NW device shows a nearly saturated mobility while the CsPbBr₃/5 nm MoO₃ NW device demonstrates increasing mobility with decreasing temperatures. This observation suggests that ion migration, polarization disorder, and phonon scattering have insignificant influence on the carrier transport, where other processes (e.g., ionized impurity scattering) become dominant limiting factors in this low-temperature regime. From a viewpoint of the surface charge transfer doping process developed in this work,

this phenomenon is possibly associated with the minimized ionized impurity (acceptor) scattering as a result of the spatial separation of the dopants from the carriers, which gives rise to the increasing hole mobility for CsPbBr₃/MoO₃ core-shell NWs at low temperatures.⁴⁴ More detailed investigations are still needed to elucidate the atomic scale mechanisms and theoretical limits of carrier mobilities in perovskite core-shell NW devices in the future.

After the successful demonstration of enhanced FET performance through surface doping, the photodetection performance of CsPbBr₃/MoO₃ core-shell NW devices was also investigated. The photodetection measurements were carried out using a 532 nm light source with a constant incident power density (P) of 1 mW/cm^2 under ambient conditions. It is profound that the photocurrent of the CsPbBr₃ device is greatly increased by $8\times$ (from 5 to 40 nA) after decorating with the 5 nm thick MoO₃ shell layer (Figure 3g). This is mainly because the MoO₃ decoration can effectively increase the n_h value of CsPbBr₃ devices without introducing any impurity scattering centers; hence, the mobility as well as photocurrent collection are significantly improved. Anyway, all devices exhibit excellent reliability in repeated on/off switching measurements at a chopping frequency of 0.2 Hz (Figure 3h). On the other hand, responsivity (R) and external quantum efficiency (EQE) are other key parameters to quantify the device performance of photodetectors. They are defined as $R = I_{\text{light}}/(PA)$ and $\text{EQE} = (I_{\text{light}}/e)/(PA/h\nu)$, where A , e , and $h\nu$ are the effective irradiated area, electronic charge, and energy of an incident photon, respectively. It is worth mentioning that the simple MoO₃ decoration on CsPbBr₃ NW devices can improve their R values from 3.33×10^2 to $2.36 \times 10^3 \text{ A/W}$ and EQE from $7.78 \times 10^4\%$ to $5.48 \times 10^5\%$, accordingly, which outperform most of the reported low-dimensional perovskite photodetectors (Table S2). Also, the fast optical response is critical for optoelectronic devices, where the response is highly dependent on the efficient charge transport and collection of

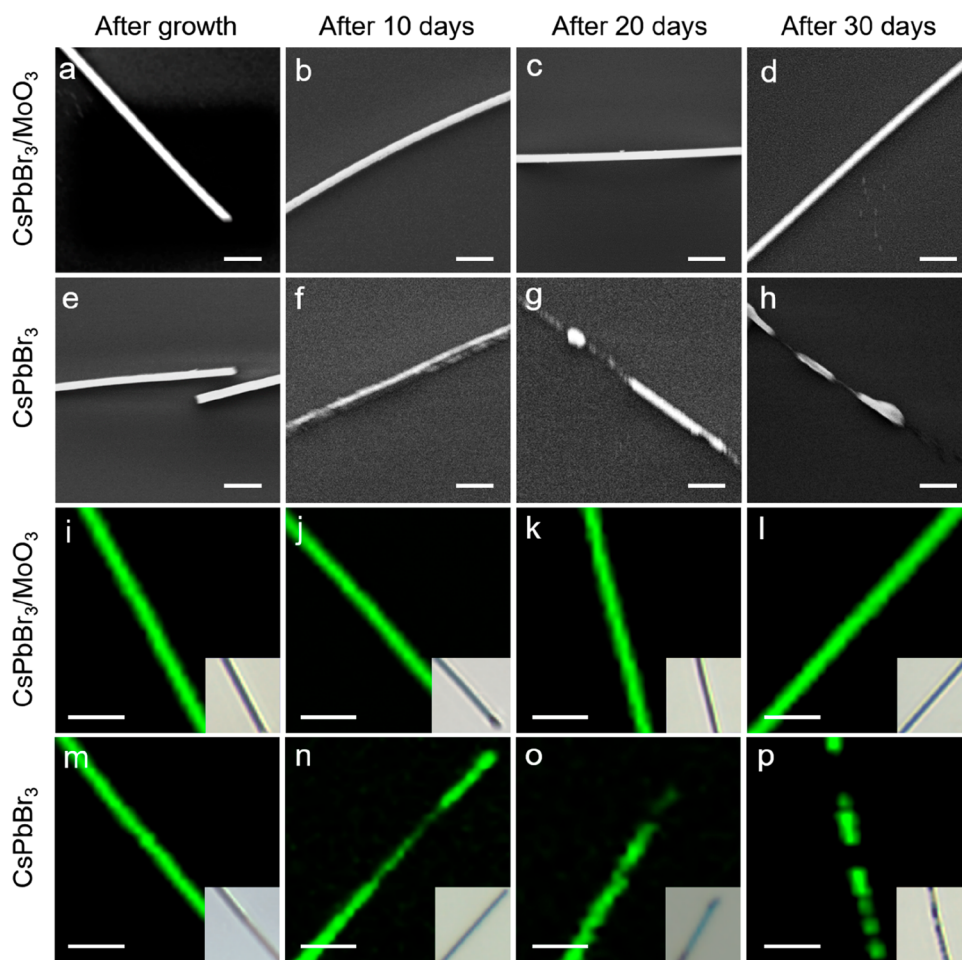


Figure 5. SEM images of (a–d) the CsPbBr₃/MoO₃ core–shell NW and (e–h) the pristine CsPbBr₃ NW with different durations of storage. Scale bars are 1 μm . Confocal PL mapping of (i–l) the CsPbBr₃/MoO₃ core–shell NW and (m–p) the pristine CsPbBr₃ NW with different durations of storage. Scale bars are 2 μm . Insets in (i)–(p) show the corresponding optical images.

devices. Figure 3i shows the temporal photoresponse of the CsPbBr₃/MoO₃ core–shell NW device at a chopping frequency of ~ 800 Hz. To bypass the smallest signal interval time ($> \text{ms}$) collected by the semiconductor parameter analyzer (Agilent 4155C), we design a photoresponse measurement circuit (Figure S19). Specifically, the light-induced current signals are first converted into voltage signals by a current amplifier, and then a digital oscilloscope is used to directly examine these dense voltage signals. The response times (*i.e.*, rise time and fall time, t_r and t_f), determined as the time for the photocurrent to vary from 10% to 90% of the peak voltage signal and *vice versa*, are found to be 230 and 280 μs , respectively. All these results clearly demonstrate an excellent performance enhancement for surface-functionalized perovskite NW photodetectors.

Surface functionalization using MoO₃ shells not only can be used to improve the electrical performance of low-dimensional halide perovskites but also has great potential to suppress the material degradation against ambient conditions (Figure 4a and b). To this end, the air stability of CsPbBr₃/MoO₃ core–shell NW FETs is thoroughly investigated by storing the devices under humid atmosphere (with a controlled relative humidity of 65% at room temperature). The representative transfer curves of different devices with different durations of storage are shown in Figure 4c (more transfer curves shown in Figure S20). After storing for 7 days, slightly reduced I_{on} (from

460 to 400 nA) and μ_{h} (from 13.3 to 10.6 $\text{cm}^2/(\text{V s})$) are observed for the CsPbBr₃/MoO₃ core–shell NW FET. In contrast, the transistor performance of the pristine CsPbBr₃ NW device is almost completely degraded after storing in the same conditions for 7 days (Figure 4d). The normalized μ_{h} of NW devices for different durations of storage under 65% relative humidity are presented in Figure 4e. The CsPbBr₃/MoO₃ core–shell NW devices show excellent long-term air stability, maintaining more than 80% of their initial mobility after 7 days, whereas the control devices based on pristine CsPbBr₃ NWs show severe performance deterioration. This stability test highlights the surface passivation of CsPbBr₃ NWs with MoO₃ shells being extremely crucial for the long-term device stability against ambient conditions.

To further assess the morphology evolution of pristine CsPbBr₃ NWs and CsPbBr₃/MoO₃ core–shell NWs under air exposure, detailed SEM studies were carried out on these two kinds of NW samples with different storing times. As opposed to the structural integrity of CsPbBr₃/MoO₃ core–shell NWs under long-time air exposure (Figure 5a–d), the pristine CsPbBr₃ NWs were found to experience severe morphological deterioration with time. For example, after storing the pristine CsPbBr₃ NWs in air for 10 days, the NW surface was roughened (Figure 5f), which represents emerging structural degradation. After prolonging the storing time to 20 days under the same condition, pronounced structural collapse of

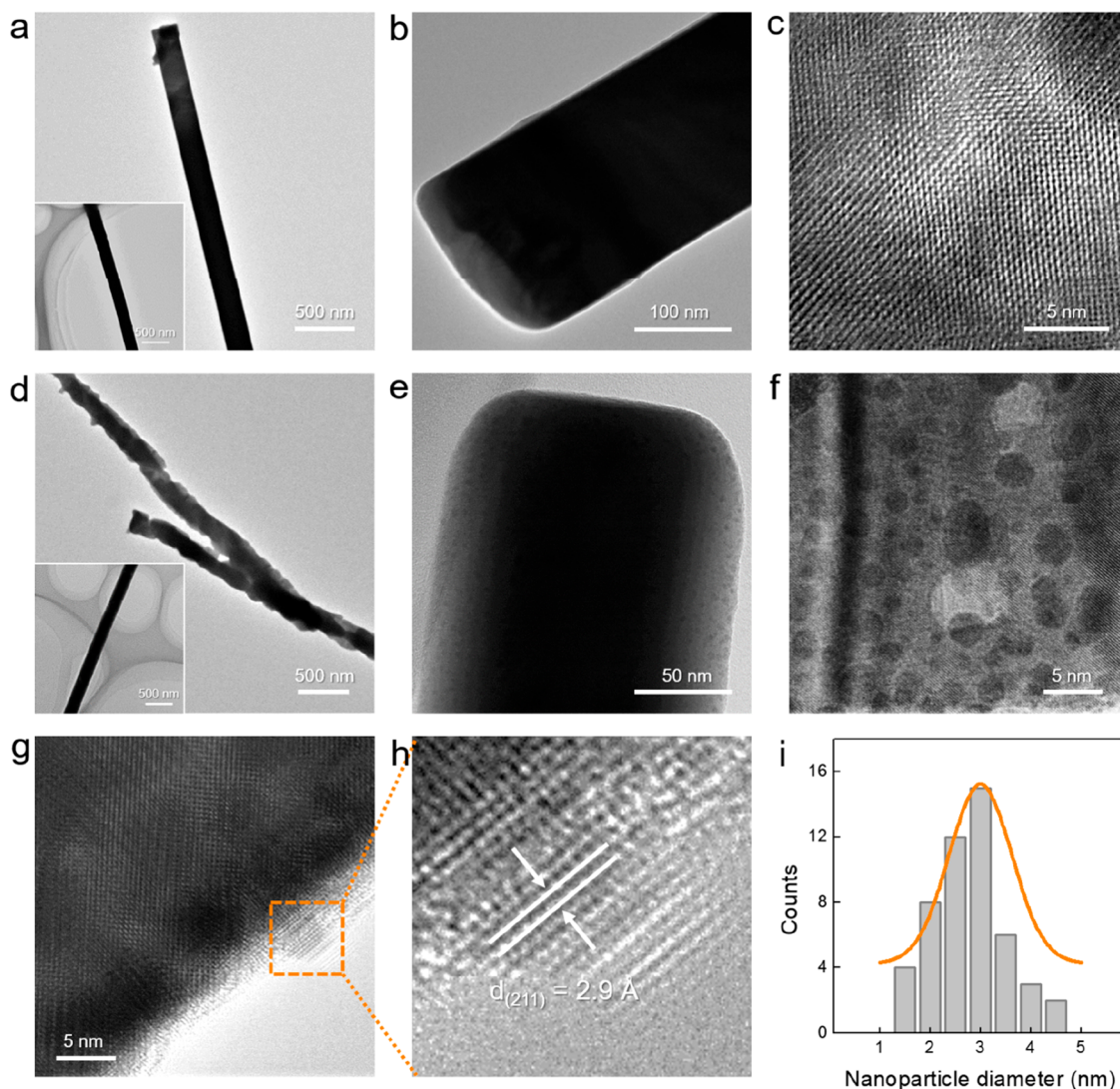


Figure 6. (a) TEM and (b, c) HRTEM images of the CsPbBr₃/MoO₃ core–shell NW after 30 days of air exposure. (Inset of a) TEM image of the CsPbBr₃/MoO₃ core–shell NW before air exposure test. (d) TEM and (e–h) HRTEM images of the pristine CsPbBr₃ NW after 30 days of air exposure. (Inset of d) TEM image of the pristine CsPbBr₃ NW before air exposure test. (i) Diameter distribution of PbBr₂ nanoparticles that generated on the pristine CsPbBr₃ NW after 30 days of air exposure.

the NW was observed as illustrated in Figure 5g. With the storing time extended to 30 days, the CsPbBr₃ NW became partly broken into short segments (Figure 5h). This distinctively different morphology evolution between pristine CsPbBr₃ NWs and CsPbBr₃/MoO₃ core–shell NWs obviously shows that the MoO₃ shell passivation is an effective strategy to improve the ambient stability of perovskites by forming kinetic barriers against the diffusion of moisture and/or atmospheric oxygen.

Apart from the SEM studies with different storing times, confocal photoluminescence (PL) mapping, a kind of non-destructive characterization technique, was also performed to evaluate the perovskite material decomposition. With the protection of the MoO₃ shell, complete and uniform PL signals can be found on the entire CsPbBr₃/MoO₃ core–shell NW body even after placing it in air for 30 days (Figure 5i–l). To some extent, this can as well prove the coverage uniformity of the MoO₃ shell. On the contrary, the pristine CsPbBr₃ NWs without any MoO₃ passivation exhibit substantially different PL mapping evolution with time under the same storage

conditions (Figure 5m–p). With the extended storing time, the PL mappings of CsPbBr₃ NWs were found to be partly darkened (Figure 5n and o, after 10 and 20 days) and then fragmented (Figure 5p, after 30 days). Overall, the PL mapping changes are perfectly consistent with the morphology evolution of NWs with different storage duration, again highlighting the passivation function of MoO₃ shells to CsPbBr₃ NW cores.

In this case, in order to study the structural degradation of NWs under environmental exposure, electron microscopy is employed to capture important nanoscale changes in their morphology and crystal structure. For pristine CsPbBr₃ NWs, after storing in ambient conditions for 30 days, the surface roughening phenomenon is evidently witnessed in the TEM image (Figure 6d). Also, dark contrast regions with an average diameter of ~ 3 nm appear on the NW surface (Figure 6e and f). These morphological changes directly indicate that the surface degradation and phase separation occurred during ambient exposure. The corresponding HRTEM images in Figure 6g and h further reveal that these dark contrast regions correspond to the (211) lattice spacing of PbBr₂ (JCPDS No.

31-0679, *Pnam*(62)). The weak PbBr_2 diffraction peak is also found in the XRD pattern of pristine CsPbBr_3 NWs after storage in air for 30 days (Figure S21). In fact, there is no evidence of CsBr crystals found in HRTEM images as well as XRD patterns. This observation is possibly associated with the different chemical bonding between Cs cations and Br anions as compared with that between Pb cations and Br anions. For example, based on a theoretical study about halide perovskites, the main type of bond between Cs and Br is ionic bonds, while it is mainly covalent bonds between Pb and Br.⁴⁵ This way, due to the chemical bond theory together with the different formation energy of PbBr_2 and CsBr , we speculate that the environmental factors trigger the structural degradation, collapsing the framework structure and accelerating the decomposition of CsPbBr_3 into nanocrystalline PbBr_2 and amorphous CsBr .^{46–48} The decomposition and recrystallization of CsPbBr_3 into its starting material of PbBr_2 is anticipated to be driven by the organization of the system into an energetically favorable state through environmental factor induced elemental diffusion.^{48–50} As a result, the morphological deterioration and presence of the PbBr_2 decomposition product under ambient exposure would have a fatal impact on the device performance. Impressively, for the $\text{CsPbBr}_3/\text{MoO}_3$ core–shell NWs, there is no observable morphological change found under the same storage conditions due to the complete surface passivation of the MoO_3 shell (Figure 6a and b). In particular, as shown in the HRTEM image in Figure 6c, the $\text{CsPbBr}_3/\text{MoO}_3$ core–shell NW keeps its clear lattice fringes that correspond to the cubic CsPbBr_3 crystal. There are no PbBr_2 nanoclusters observed on the core–shell NW surface, which is in perfect agreement with the XRD result (Figure S22). Thus, the intact morphology as well as the stabilized crystal structure guarantee the enhanced environmental stability of FET devices and thereby their outstanding device performance.

CONCLUSIONS

In summary, effective surface charge transfer doping of VLS-grown single-crystalline CsPbBr_3 NWs via surface functionalization with MoO_3 shell is reported. Utilizing this surface doping scheme, the interfacial hole injection into CsPbBr_3 NW cores would provide a high-efficiency modification to their electrical properties, manipulating the conductivity from ambipolar to dominant *p*-type and even all the way to metallic characteristics. In addition, given by the ultra-high n_h and reducing ionized impurity scattering, the hole mobility of CsPbBr_3 NW FETs is significantly enhanced to $23.3 \text{ cm}^2/(\text{V s})$ after 10 nm thick MoO_3 modification, indicating a highly improved hole transport of $\text{CsPbBr}_3/\text{MoO}_3$ core–shell NWs. Importantly, the enhanced environmental stability of devices against ambient conditions is also demonstrated as a result of the excellent passivation provided by the MoO_3 shell. All these findings can clearly indicate the surface charge transfer doping as an enabling technology to realize high-performance and air-stable perovskite nanomaterials based electronics and optoelectronics.

METHODS

Material Synthesis. All chemicals used in this work were purchased from Sigma-Aldrich. To prepare growth substrates, an aqueous suspension containing Sn nanoparticles (average particle size of 150 nm, $\geq 99\%$, Aldrich) was drop-casted onto Si/SiO₂ substrates (50 nm thick thermally grown oxide). CsBr and PbBr_2 powders were

mixed together with a molar ratio of 2:1 and then annealed at 430 °C for 30 min before placing them into the tube furnace. In a typical two-zone chemical vapor deposition (CVD) system, the heating temperature of the CsPbBr_3 source powder was 440 °C, while the growth substrates were placed into a low-temperature zone with the temperature setting of 310 °C. During the VLS growth process, mixed argon (80 sccm)/hydrogen (15 sccm) gas was used as the carrier gas, and the growth pressure was set to 1.2 Torr. After a growth duration of 180 min, CsPbBr_3 NWs with a length of 20–30 μm were obtained on the growth substrate. After NW growth, the samples were immediately moved to a thermal evaporation equipment, to avoid contamination as much as possible. To deposit MoO_3 shells, thermal evaporation under high vacuum with a nominal deposition rate of 0.5 Å/s was utilized, where the thickness of the MoO_3 layer is directly proportional to the deposition time.

Material Characterization. Scanning electron microscopy (SEM, Philips XL30) and transmission electron microscopy (TEM, Philips CM-20) were used to examine the morphologies of NWs. The crystal structures were determined by high-resolution TEM (HRTEM, JEOL 2100F) and with a Philips powder diffractometer. An energy dispersive X-ray (EDS) detector attached to JEOL 2100F was used to perform elemental mappings. To realize the elemental and chemical analysis of samples, ultraviolet photoelectron spectroscopy (UPS) as well as X-ray photoelectron spectroscopy (XPS) were employed by using a Thermo ESCALAB 250Xi system.

Device Fabrication and Characterization. Field-effect transistors with bottom-gate top-contact structure were fabricated on p^+ -Si/SiO₂ substrates (270 nm thick thermally grown oxide). To make CsPbBr_3 NWs lie down on the substrate, a contact transfer method was used to separate the NWs from the growth substrates. After that, a shadow mask with channel lengths of 10 μm was used to define the source and drain regions, and then 50 nm thick Au electrodes were deposited by thermal evaporation. FET device characterizations were performed in the dark using an Agilent 4155C semiconductor analyzer and a standard electrical probe station in atmosphere. To calculate field-effect mobility, the threshold voltage was extracted from the slope and *x*-axis intercept of the transfer curves, while the gate capacitance was obtained from COMSOL software using a cylinder-on-plane model. For photodetection measurements, a 532 nm laser diode was used as the light source, while a power meter (PM400, Thorlabs) was used to measure the incident light power.

ASSOCIATED CONTENT

Supporting Information

The Supporting Information is available free of charge at <https://pubs.acs.org/doi/10.1021/acsnano.0c03101>.

Optical images, TEM image, and SAED pattern of pristine CsPbBr_3 NWs; XPS Mo 3d spectrum and XRD pattern of MoO_3 layers; XRD patterns and EDS analysis of $\text{CsPbBr}_3/\text{MoO}_3$ core–shell NWs; output characteristics of the $\text{CsPbBr}_3/\text{MoO}_3$ core–shell NW FET; energy level values of different transition metal oxides that may be used as electron-withdrawing surface dopants; performance summary of photodetectors based on low-dimensional all-inorganic LHPs (PDF)

AUTHOR INFORMATION

Corresponding Author

Johnny C. Ho – Department of Materials Science and Engineering, State Key Laboratory of Terahertz and Millimeter Waves, and Centre for Functional Photonics, City University of Hong Kong, Kowloon 999077, Hong Kong SAR; Shenzhen Research Institute, City University of Hong Kong, Shenzhen 518057, P. R. China; Institute for Materials Chemistry and Engineering, Kyushu University, Fukuoka 816-8580, Japan;

orcid.org/0000-0003-3000-8794; Email: johnnyho@cityu.edu.hk

Authors

You Meng – Department of Materials Science and Engineering, City University of Hong Kong, Kowloon 999077, Hong Kong SAR

Zhengxun Lai – Department of Materials Science and Engineering, City University of Hong Kong, Kowloon 999077, Hong Kong SAR

Fangzhou Li – Department of Materials Science and Engineering, City University of Hong Kong, Kowloon 999077, Hong Kong SAR

Wei Wang – Department of Materials Science and Engineering, City University of Hong Kong, Kowloon 999077, Hong Kong SAR

SenPo Yip – Department of Materials Science and Engineering, State Key Laboratory of Terahertz and Millimeter Waves, and Centre for Functional Photonics, City University of Hong Kong, Kowloon 999077, Hong Kong SAR; Shenzhen Research Institute, City University of Hong Kong, Shenzhen 518057, P. R. China

Quan Quan – Department of Materials Science and Engineering, City University of Hong Kong, Kowloon 999077, Hong Kong SAR

Xiuming Bu – Department of Materials Science and Engineering, City University of Hong Kong, Kowloon 999077, Hong Kong SAR; Shenzhen Research Institute, City University of Hong Kong, Shenzhen 518057, P. R. China; orcid.org/0000-0002-2372-2271

Fei Wang – Department of Materials Science and Engineering and State Key Laboratory of Terahertz and Millimeter Waves, City University of Hong Kong, Kowloon 999077, Hong Kong SAR

Yan Bao – Department of Mechanical Engineering, City University of Hong Kong, Kowloon 999077, Hong Kong SAR

Takuro Hosomi – Department of Applied Chemistry, Graduate School of Engineering, The University of Tokyo, Tokyo 113-8654, Japan; orcid.org/0000-0002-5649-6696

Tsunaki Takahashi – Department of Applied Chemistry, Graduate School of Engineering, The University of Tokyo, Tokyo 113-8654, Japan; orcid.org/0000-0002-2840-8038

Kazuki Nagashima – Department of Applied Chemistry, Graduate School of Engineering, The University of Tokyo, Tokyo 113-8654, Japan; orcid.org/0000-0003-0180-816X

Takeshi Yanagida – Institute for Materials Chemistry and Engineering, Kyushu University, Fukuoka 816-8580, Japan; Department of Applied Chemistry, Graduate School of Engineering, The University of Tokyo, Tokyo 113-8654, Japan; orcid.org/0000-0003-4837-5701

Jian Lu – Department of Mechanical Engineering, City University of Hong Kong, Kowloon 999077, Hong Kong SAR; Shenzhen Research Institute, City University of Hong Kong, Shenzhen 518057, P. R. China; orcid.org/0000-0001-5362-0316

Complete contact information is available at: <https://pubs.acs.org/10.1021/acsnano.0c03101>

Author Contributions

The manuscript was written through contributions of all authors. All authors have given approval to the final version of the manuscript.

Notes

The authors declare no competing financial interest.

ACKNOWLEDGMENTS

We acknowledge the General Research Fund (CityU 11204618) and the Theme-based Research (T42-103/16-N) of the Research Grants Council of Hong Kong SAR, China, the National Natural Science Foundation of China (Grant 51672229), the Science Technology and Innovation Committee of Shenzhen Municipality (Grant JCYJ20170818095520778), and a grant from the Shenzhen Research Institute, City University of Hong Kong.

REFERENCES

- (1) Fu, Y.; Zhu, H.; Chen, J.; Hautzinger, M. P.; Zhu, X. Y.; Jin, S. Metal Halide Perovskite Nanostructures for Optoelectronic Applications and the Study of Physical Properties. *Nat. Rev. Mater.* **2019**, *4*, 169–188.
- (2) Li, D.; Wang, G.; Cheng, H.-C.; Chen, C.-Y.; Wu, H.; Liu, Y.; Huang, Y.; Duan, X. Size-Dependent Phase Transition in Methylammonium Lead Iodide Perovskite Microplate Crystals. *Nat. Commun.* **2016**, *7*, 11330.
- (3) Jiang, Y.; Wang, X.; Pan, A. Properties of Excitons and Photogenerated Charge Carriers in Metal Halide Perovskites. *Adv. Mater.* **2019**, *31*, 1806671.
- (4) Zhu, H.; Liu, A.; Luque, H. L.; Sun, H.; Ji, D.; Noh, Y.-Y. Perovskite and Conjugated Polymer Wrapped Semiconducting Carbon Nanotube Hybrid Films for High-Performance Transistors and Phototransistors. *ACS Nano* **2019**, *13*, 3971–3981.
- (5) Chin, X. Y.; Cortecchia, D.; Yin, J.; Bruno, A.; Soci, C. Lead Iodide Perovskite Light-Emitting Field-Effect Transistor. *Nat. Commun.* **2015**, *6*, 7383.
- (6) Li, D.; Cheng, H. C.; Wang, Y.; Zhao, Z.; Wang, G.; Wu, H.; He, Q.; Huang, Y.; Duan, X. The Effect of Thermal Annealing on Charge Transport in Organolead Halide Perovskite Microplate Field-Effect Transistors. *Adv. Mater.* **2017**, *29*, 1601959.
- (7) Zhu, H.; Shin, E. S.; Liu, A.; Ji, D.; Xu, Y.; Noh, Y. Y. Printable Semiconductors for Backplane TFTs of Flexible OLED Displays. *Adv. Funct. Mater.* **2020**, *30*, 1904588.
- (8) Wang, K.; Wu, C.; Hou, Y.; Yang, D.; Priya, S. Monocrystalline Perovskite Wafers/Thin Films for Photovoltaic and Transistor Applications. *J. Mater. Chem. A* **2019**, *7*, 24661–24690.
- (9) Huo, C.; Liu, X.; Song, X.; Wang, Z.; Zeng, H. Field-Effect Transistors Based on Van-Der-Waals-Grown and Dry-Transferred All-Inorganic Perovskite Ultrathin Platelets. *J. Phys. Chem. Lett.* **2017**, *8*, 4785–4792.
- (10) Cheng, B.; Li, T. Y.; Wei, P. C.; Yin, J.; Ho, K. T.; Retamal, J. R. D.; Mohammed, O. F.; He, J. H. Layer-Edge Device of Two-Dimensional Hybrid Perovskites. *Nat. Commun.* **2018**, *9*, 5196.
- (11) Ho, K. T.; Leung, S. F.; Li, T. Y.; Maity, P.; Cheng, B.; Fu, H. C.; Mohammed, O. F.; He, J. H. Surface Effect on 2D Hybrid Perovskite Crystals: Perovskites Using an Ethanolamine Organic Layer as an Example. *Adv. Mater.* **2018**, *30*, 1804372.
- (12) Ashley, M. J.; Kluender, E. J.; Mirkin, C. A. Fast Charge Extraction in Perovskite-Based Core-Shell Nanowires. *ACS Nano* **2018**, *12*, 7206–7212.
- (13) Strobel, P.; Riedel, M.; Ristein, J.; Ley, L. Surface Transfer Doping of Diamond. *Nature* **2004**, *430*, 439.
- (14) Lee, J.-S.; Shevchenko, E. V.; Talapin, D. V. Au-PbS Core-Shell Nanocrystals: Plasmonic Absorption Enhancement and Electrical Doping via Intra-Particle Charge Transfer. *J. Am. Chem. Soc.* **2008**, *130*, 9673–9675.
- (15) Takei, K.; Kapadia, R.; Li, Y.; Plis, E.; Krishna, S.; Javey, A. Surface Charge Transfer Doping of III-V Nanostructures. *J. Phys. Chem. C* **2013**, *117*, 17845–17849.
- (16) Kiriya, D.; Tosun, M.; Zhao, P.; Kang, J. S.; Javey, A. Air-Stable Surface Charge Transfer Doping of MoS₂ by Benzyl Viologen. *J. Am. Chem. Soc.* **2014**, *136*, 7853–7856.
- (17) Xiang, D.; Han, C.; Wu, J.; Zhong, S.; Liu, Y.; Lin, J.; Zhang, X. A.; Ping Hu, W.; Ozyilmaz, B.; Neto, A. H.; Wee, A. T.; Chen, W.

Surface Transfer Doping Induced Effective Modulation on Ambipolar Characteristics of Few-Layer Black Phosphorus. *Nat. Commun.* **2015**, *6*, 6485.

(18) Meng, Y.; Lan, C.; Li, F.; Yip, S.; Wei, R.; Kang, X.; Bu, X.; Dong, R.; Zhang, H.; Ho, J. C. Direct Vapor-Liquid-Solid Synthesis of All-Inorganic Perovskite Nanowires for High-Performance Electronics and Optoelectronics. *ACS Nano* **2019**, *13*, 6060–6070.

(19) Niu, G.; Yu, H.; Li, J.; Wang, D.; Wang, L. Controlled Orientation of Perovskite Films through Mixed Cations toward High Performance Perovskite Solar Cells. *Nano Energy* **2016**, *27*, 87–94.

(20) Zhou, H.; Yuan, S.; Wang, X.; Xu, T.; Wang, X.; Li, H.; Zheng, W.; Fan, P.; Li, Y.; Sun, L.; Pan, A. Vapor Growth and Tunable Lasing of Band Gap Engineered Cesium Lead Halide Perovskite Micro/Nanorods with Triangular Cross Section. *ACS Nano* **2017**, *11*, 1189–1195.

(21) Wang, X.; Shoaib, M.; Wang, X.; Zhang, X.; He, M.; Luo, Z.; Zheng, W.; Li, H.; Yang, T.; Zhu, X.; Ma, L.; Pan, A. High-Quality In-Plane Aligned CsPbX₃ Perovskite Nanowire Lasers with Composition-Dependent Strong Exciton-Photon Coupling. *ACS Nano* **2018**, *12*, 6170–6178.

(22) Shoaib, M.; Zhang, X.; Wang, X.; Zhou, H.; Xu, T.; Wang, X.; Hu, X.; Liu, H.; Fan, X.; Zheng, W.; Yang, T.; Yang, S.; Zhang, Q.; Zhu, X.; Sun, L.; Pan, A. Directional Growth of Ultralong CsPbBr₃ Perovskite Nanowires for High-Performance Photodetectors. *J. Am. Chem. Soc.* **2017**, *139*, 15592–15595.

(23) Zhou, C.; Zhao, Y.; Raju, S.; Wang, Y.; Lin, Z.; Chan, M.; Chai, Y. Carrier Type Control of WSe₂ Field-Effect Transistors by Thickness Modulation and MoO₃ Layer Doping. *Adv. Funct. Mater.* **2016**, *26*, 4223–4230.

(24) Li, F.-Z.; Luo, L.-B.; Yang, Q.-D.; Wu, D.; Xie, C.; Nie, B.; Jie, J.-S.; Wu, C.-Y.; Wang, L.; Yu, S.-H. Ultrahigh Mobility of P-Type CdS Nanowires: Surface Charge Transfer Doping and Photovoltaic Devices. *Adv. Energy Mater.* **2013**, *3*, 579–583.

(25) Zhao, P.; Kiriya, D.; Azcatl, A.; Zhang, C.; Tosun, M.; Liu, Y.-S.; Hettick, M.; Kang, J. S.; McDonnell, S.; KC, S.; Guo, J.; Cho, K.; Wallace, R. M.; Javey, A. Air Stable P-Doping of WSe₂ by Covalent Functionalization. *ACS Nano* **2014**, *8*, 10808–10814.

(26) Fang, H.; Tosun, M.; Seol, G.; Chang, T. C.; Takei, K.; Guo, J.; Javey, A. Degenerate N-Doping of Few-Layer Transition Metal Dichalcogenides by Potassium. *Nano Lett.* **2013**, *13*, 1991–1995.

(27) Xia, F.; Shao, Z.; He, Y.; Wang, R.; Wu, X.; Jiang, T.; Duhm, S.; Zhao, J.; Lee, S. T.; Jie, J. Surface Charge Transfer Doping via Transition Metal Oxides for Efficient P-Type Doping of II-VI Nanostructures. *ACS Nano* **2016**, *10*, 10283–10293.

(28) Russell, S. A. O.; Cao, L.; Qi, D.; Tallaire, A.; Crawford, K. G.; Wee, A. T. S.; Moran, D. A. J. Surface Transfer Doping of Diamond by MoO₃: A Combined Spectroscopic and Hall Measurement Study. *Appl. Phys. Lett.* **2013**, *103*, 202112.

(29) Verona, C.; Cicognani, W.; Colangeli, S.; Limiti, E.; Marinelli, M.; Verona-Rinati, G. Comparative Investigation of Surface Transfer Doping of Hydrogen Terminated Diamond by High Electron Affinity Insulators. *J. Appl. Phys.* **2016**, *120*, 025104.

(30) Tordjman, M.; Weinfeld, K.; Kalish, R. Boosting Surface Charge-Transfer Doping Efficiency and Robustness of Diamond with WO₃ and ReO₃. *Appl. Phys. Lett.* **2017**, *111*, 111601.

(31) Liang, J.; Zhao, P.; Wang, C.; Wang, Y.; Hu, Y.; Zhu, G.; Ma, L.; Liu, J.; Jin, Z. CsPb_{0.9}Sn_{0.1}Br₂ Based All-Inorganic Perovskite Solar Cells with Exceptional Efficiency and Stability. *J. Am. Chem. Soc.* **2017**, *139*, 14009–14012.

(32) Li, F.; Meng, Y.; Dong, R.; Yip, S.; Lan, C.; Kang, X.; Wang, F.; Chan, K. S.; Ho, J. C. High-Performance Transparent Ultraviolet Photodetectors Based on InGaN Superlattice Nanowire Arrays. *ACS Nano* **2019**, *13*, 12042–12051.

(33) Li, F.; Ma, C.; Wang, H.; Hu, W.; Yu, W.; Sheikh, A. D.; Wu, T. Ambipolar Solution-Processed Hybrid Perovskite Phototransistors. *Nat. Commun.* **2015**, *6*, 8238.

(34) Cho, N.; Li, F.; Turedi, B.; Sinatra, L.; Sarmah, S. P.; Parida, M. R.; Saidaminov, M. I.; Murali, B.; Burlakov, V. M.; Goriely, A.; Mohammed, O. F.; Wu, T.; Bakr, O. M. Pure Crystal Orientation and

Anisotropic Charge Transport in Large-Area Hybrid Perovskite Films. *Nat. Commun.* **2016**, *7*, 13407.

(35) Yu, W.; Li, F.; Yu, L.; Niazi, M. R.; Zou, Y.; Corzo, D.; Basu, A.; Ma, C.; Dey, S.; Tietze, M. L.; Buttner, U.; Wang, X.; Wang, Z.; Hedhili, M. N.; Guo, C.; Wu, T.; Amassian, A. Single Crystal Hybrid Perovskite Field-Effect Transistors. *Nat. Commun.* **2018**, *9*, 5354.

(36) Zou, X.; Liu, X.; Wang, C.; Jiang, Y.; Wang, Y.; Xiao, X.; Ho, J. C.; Li, J.; Jiang, C.; Xiong, Q.; Liao, L. Controllable Electrical Properties of Metal-Doped In₂O₃ Nanowires for High-Performance Enhancement-Mode Transistors. *ACS Nano* **2013**, *7*, 804–810.

(37) Li, D.; Lan, C.; Manikandan, A.; Yip, S.; Zhou, Z.; Liang, X.; Shu, L.; Chueh, Y.-L.; Han, N.; Ho, J. C. Ultra-Fast Photodetectors Based on High-Mobility Indium Gallium Antimonide Nanowires. *Nat. Commun.* **2019**, *10*, 1664.

(38) Wang, G.; Li, D.; Cheng, H.-C.; Li, Y.; Chen, C.-Y.; Yin, A.; Zhao, Z.; Lin, Z.; Wu, H.; He, Q.; et al. Wafer-Scale Growth of Large Arrays of Perovskite Microplate Crystals for Functional Electronics and Optoelectronics. *Sci. Adv.* **2015**, *1*, No. e1500613.

(39) Yang, T.; Wang, X.; Zheng, B.; Qi, Z.; Ma, C.; Fu, Y.; Fu, Y.; Hautzinger, M. P.; Jiang, Y.; Li, Z.; Fan, P.; Li, F.; Zheng, W.; Luo, Z.; Liu, J.; Yang, B.; Chen, S.; Li, D.; Zhang, L.; Jin, S.; Pan, A. Ultrahigh-Performance Optoelectronics Demonstrated in Ultrathin Perovskite-Based Vertical Semiconductor Heterostructures. *ACS Nano* **2019**, *13*, 7996–8003.

(40) Kagan, C.; Mitzi, D.; Dimitrakopoulos, C. Organic-Inorganic Hybrid Materials as Semiconducting Channels in Thin-Film Field-Effect Transistors. *Science* **1999**, *286*, 945–947.

(41) Matsushima, T.; Hwang, S.; Sandanayaka, A. S.; Qin, C.; Terakawa, S.; Fujihara, T.; Yahiro, M.; Adachi, C. Solution-Processed Organic-Inorganic Perovskite Field-Effect Transistors with High Hole Mobilities. *Adv. Mater.* **2016**, *28*, 10275–10281.

(42) Yusoff, A. R.; Kim, H. P.; Li, X.; Kim, J.; Jang, J.; Nazeeruddin, M. K. Ambipolar Triple Cation Perovskite Field Effect Transistors and Inverters. *Adv. Mater.* **2017**, *29*, 1602940.

(43) Senanayak, S. P.; Yang, B.; Thomas, T. H.; Giesbrecht, N.; Huang, W.; Gann, E.; Nair, B.; Goedel, K.; Guha, S.; Moya, X.; et al. Understanding Charge Transport in Lead Iodide Perovskite Thin-Film Field-Effect Transistors. *Sci. Adv.* **2017**, *3*, No. e1601935.

(44) Poncé, S.; Schlipf, M.; Giustino, F. Origin of Low Carrier Mobilities in Halide Perovskites. *ACS Energy Lett.* **2019**, *4*, 456–463.

(45) Qian, J.; Xu, B.; Tian, W. A Comprehensive Theoretical Study of Halide Perovskites ABX₃. *Org. Electron.* **2016**, *37*, 61–73.

(46) Li, Y.; Zhou, W.; Li, Y.; Huang, W.; Zhang, Z.; Chen, G.; Wang, H.; Wu, G.-H.; Rolston, N.; Vila, R.; Chiu, W.; Cui, Y. Unravelling Degradation Mechanisms and Atomic Structure of Organic-Inorganic Halide Perovskites by Cryo-Em. *Joule* **2019**, *3*, 2854–2866.

(47) Wang, K.; Yang, D.; Wu, C.; Sanghadasa, M.; Priya, S. Recent Progress in Fundamental Understanding of Halide Perovskite Semiconductors. *Prog. Mater. Sci.* **2019**, *106*, 100580.

(48) Waleed, A.; Tavakoli, M. M.; Gu, L.; Wang, Z.; Zhang, D.; Manikandan, A.; Zhang, Q.; Zhang, R.; Chueh, Y. L.; Fan, Z. Lead-Free Perovskite Nanowire Array Photodetectors with Drastically Improved Stability in Nanoengineering Templates. *Nano Lett.* **2017**, *17*, 523–530.

(49) Chen, S.; Zhang, X.; Zhao, J.; Zhang, Y.; Kong, G.; Li, Q.; Li, N.; Yu, Y.; Xu, N.; Zhang, J.; Liu, K.; Zhao, Q.; Cao, J.; Feng, J.; Li, X.; Qi, J.; Yu, D.; Li, J.; Gao, P. Atomic Scale Insights into Structure Instability and Decomposition Pathway of Methylammonium Lead Iodide Perovskite. *Nat. Commun.* **2018**, *9*, 4807.

(50) Dang, Z.; Shamsi, J.; Palazon, F.; Imran, M.; Akkerman, Q. A.; Park, S.; Bertoni, G.; Prato, M.; Brescia, R.; Manna, L. *In Situ* Transmission Electron Microscopy Study of Electron Beam-Induced Transformations in Colloidal Cesium Lead Halide Perovskite Nanocrystals. *ACS Nano* **2017**, *11*, 2124–2132.